Check for updates

Unveiling the atomistic and electronic structure of Ni^II–NO adduct in a MOF-based catalyst by EPR spectroscopy and quantum chemical modelling†

Kavipriya Thangavel, ‡[ab] Paolo Cleto Bruzzese, ‡§[ac] Matthias Mendt,¶[a]
Andrea Folli, [b] Katharina Knippen,[d] Dirk Volkmer, [d] Damien M. Murphy [b] and
Andreas Pöppl *[a]

The nature of the chemical bonding between NO and open-shell Ni^II ions docked in a metal–organic framework is fully characterized by EPR spectroscopy and computational methods. High-frequency EPR experiments reveal the presence of unsaturated Ni^II ions displaying five-fold coordination. Upon NO adsorption, in conjunction with advanced EPR methodologies and DFT/CASSCF modelling, the covalency of the metal–NO and metal–framework bonds is directly quantified. This enables unravelling the complex electronic structure of Ni^II–NO species and retrieving their microscopic structure.

Introduction

The interaction of nitric oxide with transition metal ions (TMIs) supported on microporous systems has been abundantly studied with a view of finding the relationship among bonding, stability, and reactivity of the metal–nitrosyl group.[1–6] Moreover, NO adsorption studies may reveal valuable information about the accessibility, number, chemical reactivity and electron pair acceptor strength[4,7–12] of the TMI sites as well as provide fundamental insights into the mechanism of essential processes, *e.g.* abatement of NO_x emissions.[3,4,13,14]

Infrared (IR) spectroscopy has been successfully employed to probe metal–NO adducts encapsulated in microporous materials.[2,3,15] This technique has been proved to be exceedingly powerful for revealing NO-adducts even *in operando* conditions.[16,17] However, IR spectroscopy cannot provide direct insight into the intimate features of metal–nitrosyl chemical bonding, which is particularly nontrivial to unravel.

This ambiguity arises from the close relative energy of the NO–π* orbitals compared to the d orbitals of first-row TMIs, which makes the accurate description of oxidation and/or spin state of such species difficult.[18–20]

Due to the paramagnetic nature of metal–NO adducts, electron paramagnetic resonance (EPR) spectroscopy is ideally suitable for obtaining exquisite details on the cryptic bonding of NO to transition metal centers.[1,10,11,14,21] The application of sophisticated pulse EPR techniques allows assessing the degree of covalency and spin delocalization between the metal–NO bond as well as the one with all the other ligands magnetically active, offering additional complementary insight into the electronic structure of the NO–metal ion bonding with respect of IR spectroscopies.[22,23] The subsequent reproduction of the EPR spectroscopic findings with electronic structure methods translates the experimental findings into microscopic structures enabling structure-function correlation of metal–NO species.[24–27]

While EPR investigations of NO adsorption over metal oxide surfaces and zeolites are abundant,[4–6,10,14,22,23,25,28] only a few magnetic resonance studies of such species have been reported for the metal–organic framework (MOF) compounds,[29–32] a class of microporous materials which has attracted substantial research interest within the last decades. In these systems, the coordination of NO with coordinatively unsaturated (CUS) metal ions has been probed by EPR methodologies. On one hand, weak physisorption of nitric oxide at closed-shell Al^III sites was detected in MIL-100 by observing the interaction of the unpaired electron of NO with the nuclear spin of ^{27}Al nucleus.[30] Analysis employing density functional theory (DFT) indicated that about 95–97% of the spin density is located at

[a] *Felix Bloch Institute for Solid State Physics, Leipzig University, Linnéstraße 5, 04103 Leipzig, Germany. E-mail: poeppl@physik.uni-leipzig.de*

[b] *School of Chemistry, Main building, Cardiff University, CF10 3AT, Cardiff, UK*

[c] *Department of Chemistry and NIS Centre of Excellence, University of Turin, via Giuria 9, 10125 Torino, Italy*

[d] *Institute of Physics, Chair of Solid State and Materials Chemistry, University of Augsburg, Universitätstraße 1, D-86159 Augsburg, Germany*

‡ These authors contributed equally.

§ Present address: Paolo Cleto Bruzzese – Max Planck Institute for Chemical Energy Conversion, Stiftstr. 34-36, 45470 Mülheim an der Ruhr, Germany.

¶ Present address: Matthias Mendt – SaxonQ GmbH, Emilienstr. 15, 04107 Leipzig, Germany.

15702 | *Phys. Chem. Chem. Phys.*, 2023, **25**, 15702–15714

This journal is © the Owner Societies 2023

the NO molecule and only 2–4% on the aluminium ion, underlying the weak interaction of the probe molecule with the framework metal ion.

On the other hand, thermally stable paramagnetic EPR active Ni^{II}–NO adducts occurred upon adsorption of NO at defective open-shell Ni^{II} paddle-wheel species in DUT-8(Ni). Based on their *g*-tensor, two distinct Ni^{II}–NO moieties have been identified and interpreted in terms of an axially and equatorially binding nitroxide molecule[31] and comparison with previously published investigations of Ni^{II}–NO complexes formed at the surface of Ni-doped MgO powders.[33,34] However, direct proof of this coordination motive and a deeper understanding of the corresponding electronic structure have not been presented yet.

In this work, a Ni^{II}-substituted variant of the rigid MFU-4l(large) framework family[35] comprising Ni–NO_2 coordination units[36] is adopted as a model case for the formation of Ni^{II}–NO species in a metal–organic framework. Through post-synthetic metal and side ligand exchange, the Ni^{II} ions substitute the peripheral Zn^{II} sites in the pentanuclear "Kuratowski-type" SBU, displaying five-fold coordination with three nitrogen atoms (N_f) from the SBU and two oxygen atoms from coordinating nitrite ion (see Fig. 1).[37] This leaves a potential sixth CUS site for the binding of an adsorbed nitric oxide molecule to form a stable six-fold octahedral-type coordination of the nickel ion.

First, high-field W-band continuous wave (CW) EPR spectroscopy is employed to verify the $S = 1$ electron spin state of the Ni^{II} ions in MFU-4l-NO_2 prior to NO adsorption. Subsequently, conventional X-band CW-EPR experiments are employed to reveal the formation of Ni^{II}–NO complexes upon the exposure of Ni^{II}-containing MFU-4l-NO_2 to gaseous nitric oxide. Pulse EPR experiments reveal the ^{14}N hyperfine (hf) interactions with the nitrogen nuclei N_f belonging to the first and second coordination sphere of nickel ion and with the NO allowing to assess the nature of the chemical bonding between the nickel and the different nitrogen ligands. Cutting-edge quantum chemical computations of the magnetic parameters of the five-coordinated Ni^{II} ion in the parent Ni-MFU-4l-NO_2 compound and of the Ni^{II}–NO species formed after NO adsorption translate the spectroscopic findings into atomistic structure

unravelling the unique electronic structure of nickel–nitrosyl moieties supported on a MOF platform.

Material and methods

Ni-MFU-4l-NO_2 sample preparation and structural characterization

The parent Ni-MFU-4l preparation and the side-ligand post-synthetic exchange modification were done similarly to a previously published procedure:[37] First, Ni-MFU-4l was synthesized by a post-synthetic exchange of 150 mg MFU-4l with a solution of 12 mmol $NiCl_2.6H_2O$ in 30 mL DMF at 60 °C for 20 h. The light greenish MOF was filtrated and washed with 2.5 mL DMF and MeOH. The success of the nickel exchange was proved by energy dispersive X-ray analysis (EDAX) measurement (chemical formula: $[Zn_4NiCl_4(BTDD)_3]$, where H_2-BTDD is bis(1*H*-1,2,3-triazolo[4,5-*b*],[4′,5′-*i*])dibenzo[1,4]dioxin[38]). Then, a 1 M solution of $LiNO_2$ in methanol (0.4 mL, 0.4 mmol) was added to the Ni-MFU-4l suspension (150 mg, approx. 0.12 mmol) in acetonitrile (30 mL). The mixture was stirred for 30 min at room temperature (RT), and the precipitate was filtered off and washed with methanol and CH_2Cl_2. Finally, the washed sample dried at 80 °C under vacuum, yielding 140 mg of Ni-MFU-4l-NO_2 as a greenish-yellow product with an analytically determined chemical composition $[Zn_4Ni(NO_2)_3Cl_1(BTDD)_3]$.

Powder X-ray diffraction (PXRD) pattern was recorded using Seifert XRD 3003 TT diffractometer equipped with a Meteor 1D detector at room temperature. The microstructure and stoichiometry were analysed using the scanning electron microscope (SEM – model Philips XL 30 FEG) and EDAX – model EDAX SiLi detector fitted with SEM), respectively. Fourier transform Infrared (FTIR) spectroscopy has been performed in the range 1600–400 cm^{-1} on a Bruker Equinox 55 FT-IR spectrometer.

EPR sample preparation

The CW Q- and W- band experiments on Ni-MFU-4l-NO_2 were acquired in the hydrated state. Further, The CW X-band and pulse experiments were performed on the NO-adsorbed sample in the below-mentioned condition. 4.7 mg of parent MOF was transferred into a conventional quartz glass EPR tube, and the sample was activated at 120 °C for overnight to remove the extra framework solvent/water molecules before the NO gas adsorption. After the thermal activation, the colour of the sample changed from pale green to dark yellowish green colour. Then the sample was loaded with nitric oxide (0.2 mbar) using a vacuum line at 294 K, and the NO gas was condensed into the EPR tubes by applying a liquid nitrogen cold trap to ensure that the entire amount of loaded NO was trapped within the EPR tube. After NO gas loading, the sample was immediately sealed, keeping the NO adsorbed at the parent Ni-MFU-4l-NO_2 sample in the EPR tube. Ultimately, the NO adsorbed sample was in a lite whitish-green colour.

EPR spectroscopy

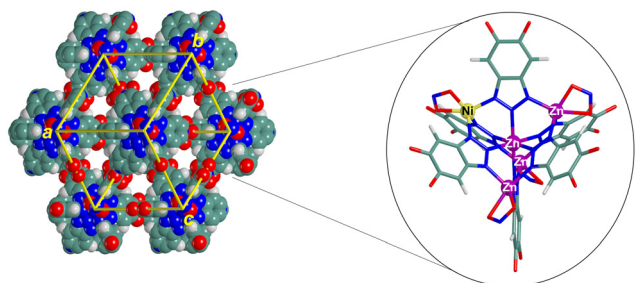CW X-band (∼9.5 GHz) EPR spectra were measured at a temperature ranging from 10 K to 288 K employing a Bruker

Fig. 1 View along the (−1 −1 −1) face of Ni-MFU-4l-NO_2 space-filling periodic model. An inset of the main subunit of the material is shown on the right. C, N, O, Ni, Zn and H are green, blue, red, yellow, violet, and white colour, respectively.

This journal is © the Owner Societies 2023

Phys. Chem. Chem. Phys., 2023, **25**, 15702–15714 | **15703**

EMXmicro spectrometer fitted with a Bruker ER4119HS cylindrical cavity using a He cryostat ESR900, Oxford instruments. The CW Q-band ($\sim$34 GHz) EPR spectrum was recorded using Bruker EMX 10–40 spectrometer fitted with a cylindrical cavity and an Oxford Instruments CF935 cryostat at T = 300 K. The high magnetic field of W-band ($\sim$95 GHz) EPR requires a superconducting magnet, Bruker 6T SC and the W-band spectra were measured at T = 20 K using an Elexsys E600 spectrometer equipped with a Bruker E600-1021H TeraFlex resonator. The EPR intensities of the X-band signals ranging from T = 10 K to T = 288 K (Fig. S5b, ESI†) were extracted by taking double integration of the full-range EPR spectrum.

The following spin Hamiltonian was used for the Ni^{II} species with spin S = 1 to interpret the Q- and W-band EPR data

$$\hat{H} = \mu_B \vec{B} \mathbf{g} \widehat{\vec{S}} + D\left[\hat{S}_z^2 - \frac{1}{3}S(S+1)\right] + E\left(\hat{S}_x^2 - \hat{S}_y^2\right) \qquad (1)$$

where the first term is the electron Zeeman interaction between S = 1 electron spins of the Ni^{II} ions and the applied external magnetic field with the Bohr magneton μ_B, the electron spin operator $\widehat{\vec{S}}$, the electron $\mathbf{g}$-tensor, and the applied external magnetic field $\vec{B}$. The second term indicates the zero-field splitting (ZFS), and D and E are the axial and rhombic ZFS parameters, respectively.

For the NO adsorption on the parent MOF, the spin Hamiltonian for the resulting Ni^{II}–NO species with spin S = 1/2 can be written as

$$\hat{H} = \mu_B \vec{B} \mathbf{g} \widehat{\vec{S}} + \sum_i \left(\widehat{\vec{S}} A_i^N \widehat{\vec{I}}_i^N + \mu_n \vec{B} g_n \widehat{\vec{I}}_i^N + \widehat{\vec{I}}_i^N Q_i^N \widehat{\vec{I}}_i^N\right). \qquad (2)$$

Here $\mathbf{g}$ is the electronic $\mathbf{g}$-tensor of the Ni^{II}–NO moiety, μ_n is the Bohr magneton of the nucleus, g_n is the ^{14}N nuclear g-factor, $\widehat{\vec{I}}_i^N$ the ^{14}N nuclear spin operator, and A_i^N and Q_i^N are the ^{14}N hf and nuclear quadrupole (nq) interactions tensors of the nitrogen of the adsorbed NO molecule and of the nitrogen atoms in the first (N$_{f1-f3}$) and second (N$_S$) coordination spheres of the triazole linkers coordinating to the Ni^{II} ion in the Kuratowski-type SBU (Fig. 7).

The EPR data were simulated by MATLAB R2019b using the EasySpin toolbox (version 6.0.0-dev36), which is based on numerical diagonalization of the spin Hamiltonian.[39] In the simulations of the CW-EPR spectra, the ^{14}N hf and nq coupling has been neglected as no nitrogen hf spitting was resolved here.

The X-band electron-spin-echo (ESE) detected EPR spectra were recorded with the pulse sequence $\frac{\pi}{2} - \tau - \pi - \tau - $ echo. The lengths of microwave (mw) pulsed $t_{\pi/2}$ = 16 ns and t_π = 32 ns, a τ value of 120 ns and a shot repetition rate of 3.55 kHz were adopted.

X-band hyperfine sublevel correlation (HYSCORE)[40] experiments were performed with the pulse sequence $\frac{\pi}{2} - \tau - \frac{\pi}{2} - t_1 - \pi - t_2 - \frac{\pi}{2} - \tau - $ echo, applying an eight-step phase cycle for deleting unwanted echoes. Pulse lengths of $t_{\pi/2}$ = 16 ns and t_π = 32 ns and a shot repetition rate of 1.77 kHz were used. The increment of the time intervals t_1 and t_2 was

16 ns giving a data matrix of 200 × 200 points; the pulse delay τ value was set to 146 ns. The time traces of HYSCORE spectra were baseline corrected with a third-order polynomial, apodized with a hamming window and zero-filled to 2048 points. After the 2D Fourier transformation, the absolute-value frequency spectra were obtained.

X-band electron nuclear double resonance (ENDOR) spectra were recorded using the Davies ENDOR pulse sequence $\pi - \pi_{RF} - \frac{\pi}{2} - \tau - \pi - \tau - $ echo.[41] Mw pulse lengths $t_{\pi/2}$ = 100 ns and t_π = 200 ns, and a radiofrequency pulse length $t_{\pi RF}$ = 10 μs, together with the mw pulse delay τ = 820 ns were employed.

Models and computational details

Periodic and cluster models. Geometry optimization and the following frequency calculations of Ni-MFU-4l-NO$_2$ structure were performed by adopting periodic boundary conditions that better describe the crystalline environment of the metal–organic framework. Starting from the purely zincous structure (space group $Fm\bar{3}m$) invented by Volkmer et al.,[42] one Zn^{II}–Cl coordination unit among the four peripheral coordination sites of each Kuratwski-type SBU was substituted by one Ni^{II}–Cl coordination unit. In this way, one Ni^{II} site was introduced per SBU, removing the cubic space group symmetry in the model (space group $P1$). Subsequently, the Cl$^-$ anions were replaced by NO$_2^-$ ligands in order to reproduce the experimental composition of the material. Adsorption of the nitric oxide molecule was simulated by positioning a NO molecule close to the peripheral Ni^{II} or Zn^{II} sites of the previously optimized structures and reoptimizing the whole adduct.

Periodic calculations have been complemented with molecular cluster calculations to compute the $\mathbf{g}$-tensor, the ZFS parameters D and E, ^{14}N hf and nq coupling tensors A_i^N, Q_i^N including the orientation of their principal axes frame with respect to the $\mathbf{g}$-tensor principal axes frame. Cluster models were cut out from the corresponding optimized periodic structures. The dangling bonds were saturated with hydrogen atoms oriented along the broken bonds to keep the local environment as in the optimized periodic models. Thus, no further geometry optimization of the cluster models was performed: the EPR parameters were computed, maintaining the same atomic coordinates as the ones in the relaxed periodic structures. The resulting net charge on the cluster models was always set to 0.

Computational details. Periodic geometry optimizations and frequencies calculations were carried out by using the massive parallel version of CRYSTAL17 code (MPPCRYSTAL)[43,44] in the frame of Density Functional Theory (DFT) adopting the hybrid B3LYP method, Becke's three parameters exchange functional and the correlation functional from Lee, Yang and Parr.[45,46] The semi-empirical dispersion corrections for the van der Waals (vdW) interactions were employed by using the Grimme approach in the so-called DFTD3 method in conjunction with a three-body correction.[47,48] The pob-TZVP-rev2 basis set[49] was used for all the elements of the MOF framework while the

15704 | *Phys. Chem. Chem. Phys.*, 2023, **25**, 15702–15714

This journal is © the Owner Societies 2023

atoms of the NO molecule were treated with Ahlrichs VTZP basis set.[50]

A pruned grid consisting of 75 radial points and a maximum number of 974 angular points in regions relevant to chemical bonding has been adopted. The accuracy of the calculation of the two-electron integrals in the Coulomb and exchange series was controlled by setting truncation criteria at the values of 10^{-7} except for the pseudo-overlap of the Hartree–Fock (HF) exchange series, which was fixed to 10^{-25}. Due to the large unit cell in the direct space, a shrink factor equal to 1 was used to diagonalize the Hamiltonian matrix in 1 k-point of the first Brillouin zone. The default value of mixing (30%) of the Kohn–Sham (KS) matrix at a cycle with the previous one was adopted. The threshold in energy variation of SCF cycles was set equal to 10^{-7} Hartree for geometry optimization and equal to 10^{-10} Hartree for frequency calculations. The number of unpaired electrons in the unit cell was locked to two for the case of Ni^{II} and to one for Ni^{II}–NO in order to guide the SCF procedure to converge to a triplet and doublet spin state of the system wavefunction, respectively.

Harmonic vibrational frequencies were computed at the center of the first Brillouin zone in the reciprocal space (Γ point) from the diagonalization of the mass-weighted Hessian matrix of the second energy derivatives with respect to atomic displacement.[51–53] One displacement for each atom along each Cartesian direction was considered to numerically compute the second energy derivatives.

Molecular cluster calculations were carried out with ORCA (v5.0.3) code.[54] The spin–orbit coupling (SOC) contribution (not negligible for Ni species)[55] was explicitly treated by using a complete mean-field spin–orbit operator (SOMF).[56] The potential was constructed to include one-electron terms, compute the Coulomb term in a semi-numeric way, incorporate exchange *via* one-centre exact integrals, including the spin-other orbit interaction and include local DFT correlation (SOC-Flags 1,2,3,1 in ORCA). Concerning the Ni-MFU-4l-NO$_2$ cluster model with Ni^{II}, ZFS and g-tensor were computed at the double-hybrid DFT level of theory by employing the B2PLYP functional.[57] The def2-QZVP basis set was employed for the Ni nucleus, while the def2-TZVPP basis sets were employed for all the other atoms.[58] Increased integration grids were employed (DefGrid3 keyword), and tight energy convergence settings were applied throughout (TightSCF keyword). The resolution of identity (RI)[59] (in conjunction with the corresponding auxiliary basis sets was adopted.[60] In case no auxiliary basis set was available, the AutoAux keyword was employed to automatically build the auxiliary basis set.[61] The "relaxed" Møller-Plesset (MP2) density was used to compute the EPR parameters, and all the electrons were kept active (NoFrozen-Core keyword). Both the spin–orbit and spin–spin contributions were taken into account for the computation of the ZFS interaction.

The *ab initio* prediction of the electronic structure for the Ni^{II}–NO adduct were based on single-point complete active space self-consistent field (CASSCF) calculations on the cluster model extracted from the optimized periodic structure. The

def2-QZVP basis set was employed for Ni, EPR-III[62] for the coordinating N nuclei, def2-TZVP[58] for the coordinating O nuclei and def2-SVP[58] for all the other atoms. The adopted active space (CAS) contains 11 electrons and 11 orbitals composed of five Ni 3d orbitals, two orbitals with predominant NO π^* character (namely π_z^* and π_y^*, where the z-axis coincides with the Ni–NO bond), one σ-type orbital that describes covalent bonding between Ni and the nitrogen atoms from the linkers and three double-shell orbitals of Ni (to describe radial correlation effects). State-averaged (SA) CASSCF calculations, including 15 doublet and 10 quartet states were adopted to optimize the active orbitals and compute the g-tensor.

^{14}N hyperfine and quadrupole couplings from the coordinating nitrogen nuclei of the first and second coordination spheres were obtained by performing a ground-state complete active space configuration interaction (CASCI) calculation of the previously optimized SA-CASSCF wavefunction. The Euler angles relative to the orientations of the ^{14}N hyperfine and quadrupole tensors were instead obtain at PBE0[58]/EPR-III level of theory.

Results and discussion

Structural analysis

PXRD obtained at 300 K (Fig. S1a, ESI†) confirms that post-synthetic ion exchanged Ni-MFU-4l-NO$_2$ is in a single phase and crystallizes within space group $Fm\bar{3}m$ (no. 225, cubic crystal system). SEM result ascertains the agglomerated particles ranging from 1 to 3 μm range (inset in Fig. S1a, ESI†). The EDAX result reveals the fraction of the post-synthetically incorporated Ni^{II}, and the ratio of Ni (20%) and Zn (80%) is found to be 1 : 4. The IR spectra result recorded between 1600–400 cm^{-1} confirms the successful formation of Ni-MFU-4l-NO$_2$ (Fig. S1b, ESI†).

CW-EPR spectroscopy and coordination geometry of Ni^{II} in Ni-MFU-4l-NO$_2$

In general, non-Kramer (integer spin) systems like the Ni^{II} ion having a d^8 electronic configuration with spin $S = 1$ are challenging to detect in EPR experiments at conventional X- and Q-band mw frequencies because of their large ZFS.[63–65] As a consequence, the allowed EPR transitions ($\Delta M_s = \pm 1$) cannot be excited by mw quanta being too small. Only a very few Ni^{II}-containing materials were characterized employing X- and Q-band EPR spectroscopy for Ni^{II} species having smaller or comparable ZFS to the MW frequency.[64–66] In order to overcome these complications, CW high-frequency EPR (HFEPR) spectroscopy techniques,[67–69] ($\sim$90 GHz to $\sim$611 GHz and magnetic fields up to $\sim$22 T) and even time-domain terahertz EPR measurements[70] were utilized to acquire the complete triplet spectrum of the $S = 1$ Ni^{II} species. Furthermore, temperature- and field-dependent magnetic susceptibility measurements also provided spin Hamiltonian parameters for such high-spin Ni^{II} systems.[63,67]

In our case, Ni-MFU-4l-NO$_2$ was first measured at Q-band frequency (see Fig. S2b, ESI†), and a part of the triplet spectrum
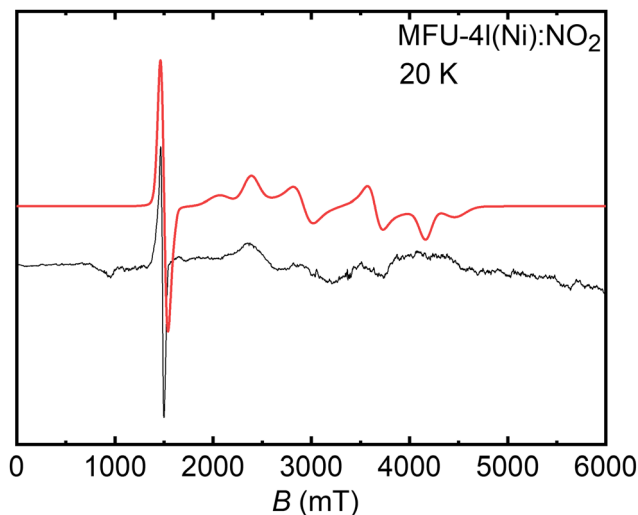
This journal is © the Owner Societies 2023

Phys. Chem. Chem. Phys., 2023, **25**, 15702–15714 | **15705**

Fig. 2 Experimental (black line) and simulated (red line) CW-EPR W-band spectrum of Ni^{II} ions having S = 1 in Ni-MFU-4l-NO$_2$ obtained at 20 K.

Fig. 3 Geometry optimized periodic structures at B3LYP-D3/pob-TZVP-rev2 of Ni-MFU-4l-NO$_2$. The computed g- and D-tensor frames are also reported.

was observed at ∼300 mT. The indication of ZFS is ambiguous to conclude the value of the ZFS of Ni^{II} species as the energy of ZFS is expected to be larger than the MW quanta energy at Q-band. To obtain the ZFS along with other spin Hamiltonian parameters, a W-band CW-EPR spectrum was recorded at 20 K (see Fig. 2). Interestingly, ZFS energy of Ni^{II} ion is not so large, and an intense forbidden transition ($\Delta M_s = \pm 2$) arose at ∼1450 mT in the W-band spectrum, whereas some poorly resolved allowed transitions ($\Delta M_s = \pm 1$) were observed at high fields 2000–4000 mT. The spin Hamiltonian parameters of the Ni^{II} species g_{xx} = 2.000, g_{yy} = 2.025, g_{zz} = 2.060, D = 35.5 GHz (1.18 cm^{-1}), and E = 0.5 GHz (0.17 cm^{-1}) are obtained by spectral simulation and suggests that the symmetry around Ni^{II} ion is slightly rhombic. Fig. S3 (ESI†) shows the angular dependences of the Ni^{II} EPR signals computed with the derived spin Hamiltonian parameters at W- and Q-band frequencies, confirming the assignment of the signals observed at about 1450 mT at W-band (Fig. S3a, ESI†) and 300 mT at Q-band (Fig. S3b, ESI†) to the $\Delta M_s = \pm 2$ transition and the consistency of both experiments.

It is well-known that zero-field splitting is intrinsically connected with the geometric structure of Ni^{II} complexes and originated from the spin–spin interactions mediated by the ligand field and from the spin–orbit coupling.[68,70] While relatively small ZFS values were reported for octahedral Ni^{II} complexes,[71–74] larger ZFS parameters occur for tetrahedral coordination.[69,75] Hence, the estimated values of D and E for Ni^{II} ions in Ni-MFU-4l-NO$_2$ may be used to retrieve peculiar details on the five coordination-based atomistic structures of the Ni^{II} paramagnetic center, as discussed below.

To transpose the spectroscopic results extracted from the analysis of W-band experiment into a microscopic structure, *ab initio* calculations of the g-tensor and ZFS were performed on the optimized structure of Ni^{II}-MFU-4l reported in Fig. 3. The Ni^{II} ion occupies a single peripheral site of the Kuratowski-type SBU displaying a five-fold coordination with three lattice

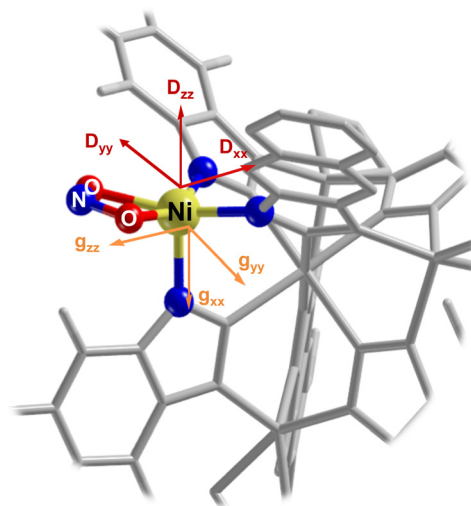nitrogen atoms and two oxygen atoms from the NO$_2^-$ ligand. The Ni–O bond lengths are slightly longer (≈0.27 nm) as compared to the Ni–N bond lengths (≈0.20 nm). A quantitative analysis from EDAX results indicates that the amount of Ni in the material is 22.5% in atomic weight (and 21% in molar weight) in comparison with Zn^{II} centers, justifying the assumption of considering only one Ni^{II} site per one SBU in the model.

Although DFT calculations of the ZFS often fail to arrive at the correct sign and magnitude of D and/or E parameters,[76,77] the computed D and E parameters obtained at B2PLYP/def2-QZVP level of theory are in good agreement with the experimental ones (see Table 1). The superiority of double-hybrid functionals with respect to more common hybrid functionals lies in a better description of the excited states of different multiplicities, which contribute significantly to the ZFS parameters.[78] The prevalent source of computed ZFS arises from the spin–orbit coupling effect, in agreement with other open-shell transition metal ions.[79] The calculated spin–spin contribution accounts only for 0.3% for D and 9% for E parameters. For comparison, a tetrahedral Ni^{II} ion in the Ni-MFU-4l model with a Cl$^-$ ligand (see Fig. S4b, ESI† and Table 1) instead of NO$_2^-$ provides an axially symmetric g- and ZFS tensor with D parameter that is further overestimated with respect to the experimental value, validating the five-coordinated structure presented in Fig. 3. Otherwise, a slightly rhombic g-tensor is predicted from the calculations

Table 1 Experimental and computed spin Hamiltonian parameters for spin S = 1 Ni^{II} incorporated in different Ni-MFU-4l-X framework variants. Uncertainty values for the g_{ii}, D, and E/D parameters of 0.006, 0.01 cm^{-1} and 0.01 were estimated for the experimental values, respectively

	Geometry (ligand X)	g_{xx}	g_{yy}	g_{zz}	D (cm^{-1})	E/D
Computed	Four-coordinated (Cl)	2.186	2.186	2.194	1.62	0.01
	Five-coordinated (NO$_2$)	2.133	2.175	2.191	1.53	0.09
Experimental		2.000	2.025	2.060	1.18	0.14

15706 | *Phys. Chem. Chem. Phys.*, 2023, **25**, 15702–15714

This journal is © the Owner Societies 2023

for Ni-MFU-4l-NO$_2$ model (Table 1) consistent with the experimental values.

To summarize, the analysis of the W-band spectrum evidences the presence of Ni^{II} species incorporated within the Ni-MFU-4l-NO$_2$ framework *via* post-synthetic ion exchange modification. The microscopic structure of such Ni^{II} centers is retrieved by comparing the experimental spin Hamiltonian parameters, in particular the ZFS, with the computed ones, and it may be ascribed as five-coordinated Ni^{II} ion located on one of the peripheral sites of the SBUs of the Ni-MFU-4l-NO$_2$. Additionally, in complement with the EPR analyses, IR spectra for the Ni-MFU-4l-NO$_2$ and Ni-MFU-4l-Cl complexes are consistent with the spectra extracted from the DFT calculations (Fig. S10, ESI†).

CW and pulse EPR investigations of the Ni^{II}–NO adduct in Ni-MFU-4l-NO$_2$

Interaction of the thermally activated Ni-MFU-4l-NO$_2$ with adsorbed NO was initially monitored by CW-EPR. The recorded X-band EPR spectra at 10 K and 288 K are shown in Fig. 4 and display the appearance of an intense EPR signal upon adsorption of nitric oxide over Ni-MFU-4l-NO$_2$. The complete set of temperature-dependent ($\Delta T = \sim 25$ K) EPR data ranging from 10 K up to 288 K is given in Fig. S5a and Table S1 (ESI†). The signal intensity and linewidth increase with higher NO loading (Fig. S12, ESI†). Spectral simulations reveal that the spectra in Fig. 4 are composed of a superposition of a major species A (93% signal contribution) with principal values of its g-tensor given in Table 2 and a minor species B (7% signal contributions) with principal values $g_{xx,yy} = 2.296$, $g_{zz} < 2.224$. The EPR signal intensity follows the expected $1/T$ behavior of a paramagnetic system according to Curie's law (Fig. S5b, ESI†). Both, g_{ii}-values and linewidths, exhibit a weak temperature dependence, which is presented and discussed in Fig. S6 and S7 (ESI†). The obtained g-values for species A and B, $g_{ii} > g_e$, where $g_e = 2.0023$ is the g-value of the free electron, indicate that the unpaired electron resides in a 3d^9 orbital of the Ni^{II} ion[33,34] of

the Kuratowski-type SBU and is not localized in the antibonding π_z^* orbital of the adsorbed NO molecule. The latter case has been typically observed for nitric oxide physisorbed on metal oxide surfaces, in zeolites, and MOFs with CUS sites at closed-shell metal ions, where $g_e \geq g_{ii}$ holds.[1] Moreover, the EPR spectra of these NO adsorption complexes are usually not detectable at room temperature because of the small adsorption energies of the nitric oxide molecules.[8,9,11–14,19–21]

The observed paramagnetic 3d^9 ground state of the Ni^{II}–NO adsorption complex has been interpreted in terms of a Ni^I–NO$^+$ species[33,34] or by an AFM coupled Ni^{II}–NO adduct,[33,34] where the later assignment has been strongly supported by recent quantum chemical computations.[33,34] In the following, we will restrict our discussion to the major species A and assign the minor species B to a Ni^{II}–NO adsorption complex, which is formed at nickel ion associated with a structural defect of the MOF framework or at a residual four-coordinated tetrahedral Ni^{II} ion with a Cl$^-$ ligand being left from the initially synthesized Ni-MFU-4l material. However, as this minor species B accounts for only 7% of the total Ni^{II} it cannot be identified in the W band spectra of Ni-MFU-4l-NO$_2$ (Fig. 2), and unambiguous assignment is not possible.

According to second-order perturbation theory, a (d$_{x^2-y^2}$) ground state leads to principal values of the g-tensor[80–82]

$$g_{xx,yy} \approx g_e + \frac{2\lambda}{\Delta_{1,2}}; \quad g_{zz} \approx g_e + \frac{8\lambda}{\Delta_3} \qquad (3)$$

reflecting the symmetry of the experimentally obtained g-tensor $g_{zz} > g_{xx,yy} > g_e$ of the Ni^{II}–NO species A. Here, λ is the spin–orbital coupling constant of the Ni^{II} ion (315 cm^{-1}), Δ_1 and Δ_2 are the energy splitting between the (3d$_{x^2-y^2}$) ionic ground state accommodating the unpaired electron and the (3d$_{yz}$) and (3d$_{xy}$) excited states, whereas Δ_3 corresponds to the energy difference between the ground state and the (3d$_{xy}$) excited state. Therefore, having an unpaired electron in the (3d$_{x^2-y^2}$) nickel atomic orbital (AO), an AFM coupling between the adsorbed NO molecule and the Ni^{II} ion can be established by the interaction
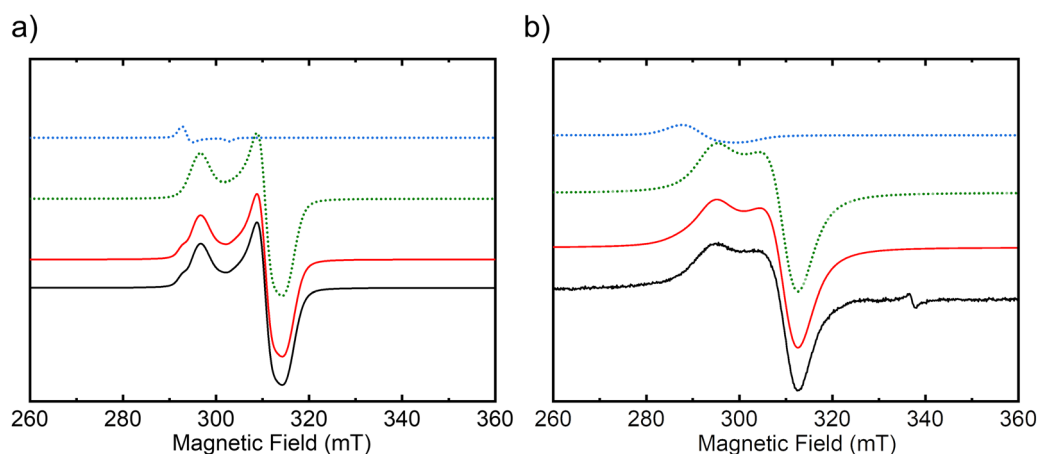

Fig. 4 Experimental (black lines) and simulated (red lines) X-band CW-EPR spectra of the Ni^{II}–NO adduct in Ni-MFU-4l-NO$_2$ formed upon NO adsorption and recorded at (a) 10 K and (b) 288 K. The simulation is composed of the sum of two different species A (dotted green line) and B (dotted blue line). The small signal around ∼340 mT corresponds to the radical.

This journal is © the Owner Societies 2023

Phys. Chem. Chem. Phys., 2023, **25**, 15702–15714 | **15707**

Table 2 Computed and experimental spin Hamiltonian parameters for the prevalent Ni^{II}–NO species in Ni-MFU-4l-NO$_2$. The labels of the nuclei refer to the ones reported in Fig. 7. Hyperfine and quadrupole couplings are given in MHz. Uncertainty values for the **g**-, **A**-tensors, e^2qQ/h and η of 0.005, 0.5 MHz, 1.5 MHz and 0.4 were estimated for the experimental values, respectively. For the simulation of the spectra, the computed g-frame and Euler angles for **A**- and quadrupole tensors were adopted

	g-Tensor						**^{14}N A-tensor**		**^{14}N Q-tensor**	
Experimental	g_{xx}	g_{yy}	g_{zz}				a_{iso}	$\lvert T \rvert$	$\lvert e^2qQ/h \rvert$	η
	2.136	2.167	2.270	Strongly coupled	^{14}N(1)		−3.0	13.0	2.7	0.8
					^{14}N(2)		11.0	1.5	3.2	0.6
				Weakly coupled	N$_s$		1.0	0.4	3.2	0.8
Computed	2.226	2.255	2.276		N$_{NO}$		−3.9	11.0	5.0	0.3
					N$_{f1}$		9.9	1.3	4.7	0.5
					N$_{f2}$		9.6	1.3	4.6	0.4
					N$_{f3}$		8.0	1.1	4.3	0.4
					N$_s$		0.6	0.3	5.8	0.5

of the unpaired electrons in the antibonding π_z^* molecular orbital of the NO and the $3d_{z^2}$ AO of the nickel ion in leading to a $(d_{yz})^2(d_{xz})^2(d_{xy})^2(d_{x^2-y^2})^{\uparrow}_{(d_{z^2})}{}^{\uparrow}{}_{(\pi_z^*)}{}^{\downarrow}$ ground state configuration of the Ni^{II}–NO moiety.[33,34]

The lack of ^{14}N hyperfine structure in the CW-EPR spectra indicates that the spin density is predominantly based on the nickel ion. As a result of this, the hyperfine interactions from the N nuclei of the organic linker and NO are small, and the information is hidden in the inhomogeneously broadened line of the CW-EPR spectrum. To recover the missing couplings arising from ^{14}N ($I = 1$), and obtain details on the local coordination environment of the Ni^{II}–NO species, pulse EPR measurements (HYSCORE and ENDOR) were carried out at X-band.

Orientation-selective ^{14}N Davies ENDOR spectra of Ni^{II}–NO in MFU-4l-NO$_2$ are reported in Fig. 5. An ENDOR signal represents an NMR absorption which is observed as a change in the echo signal intensity at a fixed resonant magnetic field, B_0. The ENDOR pattern for the $\Delta m_I = \pm 1$ transitions for ^{14}N ($I =1$), are expected to obey the following equation for the nuclear transition frequencies of the electron spin manifolds with α and β corresponding to $M_s = \pm 1/2$

$$\nu_{\alpha,\beta}(m_I \leftrightarrow m_I + 1) = \lvert A/2 \pm \nu_I + 3Q(m_I - 1/2)\rvert \quad (4)$$

where A and Q are the orientation-dependent hyperfine and quadrupole interaction constants, depending on the tensors A_i^N and Q_i^N, and the orientation of the external magnetic field, respectively, and $\nu_I = 1.00$ MHz is the nuclear Larmor frequency of ^{14}N at X-band.[83] In a strong coupling regime ($\lvert A \rvert > 2\lvert \nu_I \rvert$), as occurs in this case, the equation describes a pattern consisting of two groups of $2I$ lines each, centered at $A/2$ and separated by $2\nu_I$. Within each group, the resonances are separated by $3Q$.

The low field ^{14}N ENDOR spectrum of Ni^{II}–NO in MFU-4l-NO$_2$ (Fig. 5) corresponds to a single crystal-like orientation and is characterized by an unresolved set of $2I = 2$ quadrupole lines separated by $2\nu_I$ and centered at a frequency corresponding to $A/2$. The quadrupole splitting is partially resolved at higher fields generating complex ENDOR spectra. Spectral features at 320 mT and 325 mT suggest the existence of two sets of ^{14}N nuclei, one with a larger hyperfine coupling (contributing especially to the high-frequency part of the spectra, hereafter named ^{14}N(1)), the other with a smaller coupling responsible for the splitting structure in the low-frequency region (hereafter referred to as ^{14}N(2)). This assignment was confirmed by a simulation analysis, which proved impossible to convincingly fit simultaneously the spectra recorded at three field positions with a single nitrogen species. The involvement of two interacting ^{14}N species dramatically complicates the simulation procedure by increasing the number of unknown parameters. For this reason, the relative orientations of the quadrupole coupling and hyperfine coupling tensors with respect to the **g**-tensor principal axes frame were fixed from DFT calculations (*vide infra*). Careful scrutiny of the ENDOR spectra evinced that the ^{14}N(2) signal is given by multiple nitrogen nuclei possessing comparable magnitude of hyperfine and quadrupole couplings but slightly different orientations of the corresponding $A_{1,2}^N$ and $Q_{1,2}^N$ tensors with respect to the **g**-tensor. Nevertheless, the spectral resolution does not allow to completely disentangle nitrogen nuclei magnetically equivalent but with different orientations of the hyperfine and quadrupole tensors. Simulations of the field-dependent ENDOR spectra allowed to extract
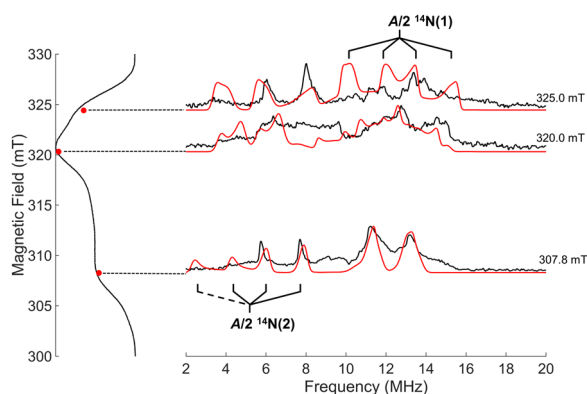
Fig. 5 Experimental (black) and simulated (red) X-band ^{14}N ENDOR spectra of Ni^{II}–NO adduct in Ni-MFU-4l-NO$_2$ recorded at different magnetic field settings. The simulation of the ^{14}N(2) signal was obtained by using one of the DFT-computed set of Euler angles for the triazole ^{14}N. The ESE spectrum with the corresponding field positions at which the ENDOR spectra were taken is plotted on the left-hand side. All spectra were recorded at 10 K.

15708 | *Phys. Chem. Chem. Phys.*, 2023, **25**, 15702–15714

This journal is © the Owner Societies 2023

of the principal values of the ^{14}N tensors $A_{1,2}^N$ and $Q_{1,2}^N$. The ^{14}N hf interaction tensors are found to be axially symmetric within the accuracy of the simulation procedure, and the corresponding isotropic Fermi contact (a_{iso}) and dipolar (T) hf coupling parameters[83] are given in Table 2 (for further details, see Table S2, ESI†). The sign of the principal values of tensors $A_{1,2}^N$ was assigned according to the *ab initio* calculations. The estimated nq interaction tensors are rhombic and presented in terms of the nq coupling parameter e^2qQ/h and the rhombic distortion parameter η.[83] The contribution from the different species was properly weighted in the simulation in order to fit better the experimental plot (^{14}N(1) and ^{14}N(2) species were considered in 1:1 ratio).

The decomposition of the ^{14}N hfi tensors a_{iso} and T components allows to the extraction of exquisite information on the nature of Ni–N chemical bonding. The dominant a_{iso} contribution in the ^{14}N(2) hf coupling tensor implies a large s-character of the Ni–^{14}N(2) bonds diagnostic for a prevalent σ-type bonding. On the other hand, the ^{14}N(1) hf interaction is dominated by the dipolar T contribution pinpointing to a main p-character of the Ni–^{14}N(1) bond. The degree of spin delocalization in the 2s (ρ_s) and 2p (ρ_p) orbitals of the two different nitrogen species may be derived from the extracted hf couplings. By using the atomic parameters for nitrogen ($a_0 = 1540.33$ MHz and $b_0 = 127.22$ MHz)[84] and considering a unitary spin density in the 2s and 2p orbitals, $\rho_s = 0.003$ and $\rho_p = 0.10$ for N(1) while $\rho_s = 0.007$ and $\rho_p = 0.012$ for N(2). These values clearly reflect the substantial p-character of the Ni–N(1) bond with respect to the Ni–N(2) bond.

The X-band HYSCORE spectra of NO adsorbed Ni^{II}-MFU-4l-NO$_2$ recorded at three field positions are reported in Fig. 6. In ^{14}N HYSCORE spectra, the correlation peaks (ν_α, ν_β) and (ν_β, ν_α) are further split into multiplets due to the nq interaction. In this case, the ^{14}N hyperfine interaction detected by HYSCORE experiments is approximately twice the nitrogen

Larmor frequency at X-band frequency, leading to the so-called cancellation regime.[85] Therefore, the transitions detected are assigned to ^{14}N nuclei weakly coupled to the Ni^{II}–NO adduct, likely located on the second coordination sphere. Cross peaks at (± 1.6, $+4.2$) and (± 4.2, $+1.6$) MHz are assigned to (ν_-, ν_{DQ}) frequencies, the signals at ($+3.2$, $+4.2$) and ($+4.2$, $+3.2$) MHz correspond to (ν_+, ν_{DQ}) and (ν_{DQ}, ν_+) frequencies while the low-frequency ridges at (± 0.6, $+1.6$) and (± 1.6, $+0.6$) may be assigned to (ν_0, ν_-) frequencies. An additional feature appearing at about 4 MHz in the spectra is due to the nuclear double-quantum transition frequency (ν_{DQ}) of the other electron spin manifold. The full set of spin Hamiltonian parameters for such weakly coupled nitrogen nuclei (N$_s$) were recovered by fitting the HYSCORE spectra simultaneously at three magnetic fields and are likewise summarized in Table 2.

Summarizing, the combination of CW-EPR and hyperfine techniques provide evidence that, upon NO adsorption on Ni^{II}-MFU-4l-NO$_2$ material, a Ni^{II}–NO adduct is formed in which the spin density is prevalently located at the nickel center. The absence of resolved ^{14}N hyperfine splitting in the CW-EPR spectra points out that only minute spin density is retained on the NO moiety and N ligands from the Ni-MFU-4l-NO$_2$ framework. Therefore the NO binding mode to the Ni^{II} ion occurs *via* the following spin pairing mechanism NO↑ + Ni^{II}↑↑ → [↑Ni^{II}(↑ ↓)NO], as it was previously proposed on other systems containing metal–nitrosyl bonding.[6,14,86–88] Most importantly, hyperfine techniques allowed us to detect the hidden ^{14}N hf interaction from coordinating nitrogen ligands. In a complementary fashion, HYSCORE experiments indicate the presence of remote nitrogen atoms belonging to the second coordination sphere of the Ni^{II}–NO species. In contrast, ENDOR measurements indicate the presence of two magnetically inequivalent nitrogen species directly linked to the Ni ion, each of them displaying a different degree of covalency of the Ni–N chemical bond.

Geometric and electronic structure of Ni^{II}–NO in MFU-4l-NO$_2$

It is widely established that NO binds transition metal centers through the nitrogen atom.[18] In metal–nitrosyl complexes, the NO character may range from that of a nitrosyl cation (NO$^+$), which binds to the metal with a metal–NO angle of about 180°, to that of a nitrosyl anion (NO$^-$), for which a bond angle of about 120° might be predicted. The occurrence of the former case instead of the latter depends on the amount of electron density donated from the antibonding orbital of NO to the metal 3d orbital and *vice versa* (σ-donation/π-back donation). A generalized description of the metal–NO bonding mechanism is provided by the {MNO}^{n} formulation proposed by Feltham and Enemark,[89,90] where M is the metal center and n is the sum of the metal d-electrons and the nitrosyl π* electrons. For instance, for a six-coordinated complex with $n = 9$, like our case, the metal–N–O angle is predicted to be bent.[89–91]

The adsorption of NO on the peripheral Ni^{II} site of Ni-MFU-4l-NO$_2$ was modelled by exploiting periodic boundary conditions, and the optimized geometry is shown in Fig. 7. The computed absolute adsorption energy of NO to Ni^{II} site
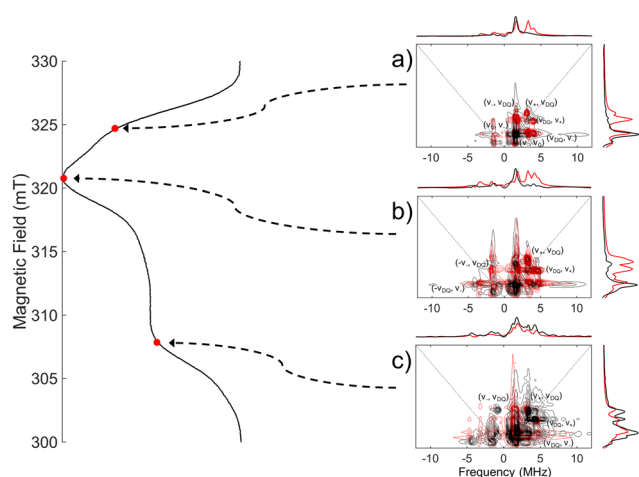
Fig. 6 Simulation (in red) of the X-band ^{14}N HYSCORE spectrum (in black) of Ni^{II}–NO adduct in Ni-MFU-4l-NO$_2$ recorded at (a) 325.0 mT, (b) 320.8 mT, and (c) 309.0 mT. The ESE detected EPR signal of Ni^{II}–NO is reported on the left side. Spectra were recorded at 10 K.

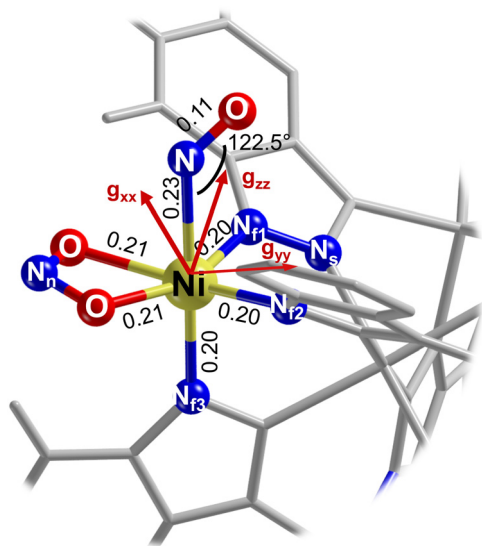This journal is © the Owner Societies 2023

Phys. Chem. Chem. Phys., 2023, **25**, 15702–15714 | **15709**

Fig. 7 Atomistic structure of Ni^{II}–NO species in Ni-MFU-4l-NO$_2$ as obtained after the geometry optimization of the periodic model. The labels of the significant nuclei are reported. The relevant bond lengths are given in nm. The computed **g**-tensor orientations are shown in red.

(ΔE_{ads} = 31.0 kJ mol^{-1}) is higher in absolute value than that of NO on the peripheral Zn^{II} ions (ΔE_{ads} = 12.0 kJ mol^{-1}, see also Fig. S8, ESI†), validating the appearance of nickel species in the X-band EPR spectra upon NO adsorption. The computed adsorption energy ΔE_{ads} = 31.0 kJ mol^{-1} is in the range of the activation energy E_{A2} = 23(1) kJ mol^{-1} determined from the temperature dependence of the homogeneous line width of the CW-EPR signal of the Ni^{II}–NO adduct at higher temperatures (Fig. S7, ESI†). Thus, we may speculatively relate the homogeneous line broadening of the EPR signal at elevated temperatures to the onset of the desorption progress of the nitric oxide molecules from the Ni^{II} ions, as already observed for other NO adsorption complexes.[33,34] The formation of Ni^{II}–NO adduct leads to a pseudo-octahedral geometry in which the Ni–N–O bond angle is slightly bent (122.5°), as predicted by Walsh-type diagrams.[89,90] The parent Ni–N$_f$ and Ni–O bonds are utterly preserved, and their length underwent a small increase with respect to the values for the five-coordinated nickel ion, especially the Ni–N$_{f3}$ distance (Fig. 7). The major elongation of the Ni–N$_{f3}$ bond is consistent with the weakening of the metal–ligand bond trans to the nitrosyl predicted by the {MNO}^{n} model for a six-coordinated complex.[92] Similar structural changes were reported for porphyrin systems.[93,94] The N–O bond length (0.11 nm) of the nitric oxide ligand is slightly shorter than the one relative to the gas-phase value. The reduction of the N–O bond length is a clear reflection of the depopulation of the antibonding π* orbital, which contains the unpaired electron in the NO molecule.

Nevertheless, a detailed depiction of the electronic structure of nickel–nitrosyl complexes may not be accurately described by means of widely used approximate DFT methods. Indeed, the open-shell 3d^8 configuration of Ni^{II}, along with the "non-innocent" NO ligand, generates a multiconfigurational

character in the Ni^{II}–NO electronic structure, extensively observed in the case of the nitrosyl ligands.[14,88,95–99] Therefore, CASSCF calculations have been employed adopting an active space composed of 11 electrons and 11 orbitals (11e,11o), which involves all the 3d Ni orbitals, the NO π* orbitals, the σ-bonding orbitals describing the covalent bonding with the framework of the Ni-MFU-4l-NO$_2$ and the nitrite ligand and three 4d Ni orbitals.

A graphical representation of some of the CAS-optimized natural orbitals is given in Fig. 8 (see Fig. S11, ESI† for the visualization of the complete set of orbitals). The bonding between Ni and NO is based on a σ-type bond composed of the bonding (d$_z^2$ + π$_z$*) and the antibonding (d$_z^2$ − π$_z$*) molecular orbitals (the cluster model was oriented in order to have the z-axis passing through the Ni^{II}–NO bond). The σ-bonding orbital is mainly represented by the Ni 3d$_z^2$ (≈ 86%) orbital, while the σ-antibonding orbital is composed of the NO π$_z$* (≈ 58%), π$_y$* (≈ 23%) and Ni 3d$_z^2$ (≈ 5%) orbitals. The different contributions of the Ni- and NO-based fragment orbitals into the bonding and antibonding natural orbitals indicate the presence of non-negligible ionic components in the Ni–NO σ-bond.

CASSCF calculations correctly predicted a doublet (S = 1/2) ground state, in line with the experimental evidence. The most representative contribution to the Ni^{II}–NO electronic structure is provided by the Ni^{II}(S = 1)–NO^0(S = 1/2) resonance structure (85.1%) with the following electronic configuration: (d$_{yz}$)^2(d$_{xz}$)^2(d$_{xy}$)^2 (d$_{x^2-y^2}$)$^\uparrow$(d$_z^2$)$^\uparrow$(π$_z$*)$^\downarrow$. Such configuration describes the antiferromagnetic coupling between the unpaired electrons on the Ni^{II} 3d$_z^2$ orbital and the NO π$_z$* orbital. Thereby, its dominant role entirely agrees with the proposed spin pairing mechanism of the NO binding. The remaining contributions to the Ni^{II}–NO ground state are given by Ni^I(S = 1/2)–NO$^+$(S = 0) with an electronic configuration of (d$_{yz}$)^2(d$_{xz}$)^2(d$_{xy}$)^2(d$_z^2$)^2(d$_{x^2-y^2}$)$^\uparrow$ and Ni^{III}(S = 1/2)–NO$^-$(S = 0) with an electronic configuration of (d$_{yz}$)^2(d$_{xz}$)^2(d$_z^2$)^2(d$_{x^2-y^2}$)$^\uparrow$(d$_{xy}$)$^\uparrow$(π$_z$*)$^\downarrow$, which account for 8.9% and 1.3%, respectively. The larger contribution of the cationic resonance structure with respect to the anionic one agrees well with the NO$^{\delta+}$ formulation of the nitrosyl moiety, already reported in other precedented studies.[14]

The SOMO of the doublet spin state is mainly a Ni 3d$_{x^2-y^2}$ orbital with a slight overlap with the hybrid sp orbitals of the N$_f$ and O atoms of the NO$_2$ ligand. The calculated spin density exhibits a positive region predominantly localized on the nickel center, with minute portions on the N$_f$ and O atoms of the NO$_2$ ligand. On the other hand, a negative spin density is predicted on the nitrosyl ligand (Fig. 8, at the bottom) due to the effective polarization induced by the unpaired electron spin density in the 3d$_{x^2-y^2}$ orbital perpendicular to the Ni–NO bond. Given the positive gyromagnetic ratio γ of the ^{14}N nuclear spin, a negative contribution of the spin distribution in the nitrogen 2s orbital corresponds to a negative hf interaction. This is indeed the case of the N atom of NO. On the contrary, a positive hf interaction is calculated for N$_f$ atoms because of a direct spin density transfer via the overlap of the hybrid sp orbitals of N$_f$ atoms with the Ni 3d$_{x^2-y^2}$ orbital.
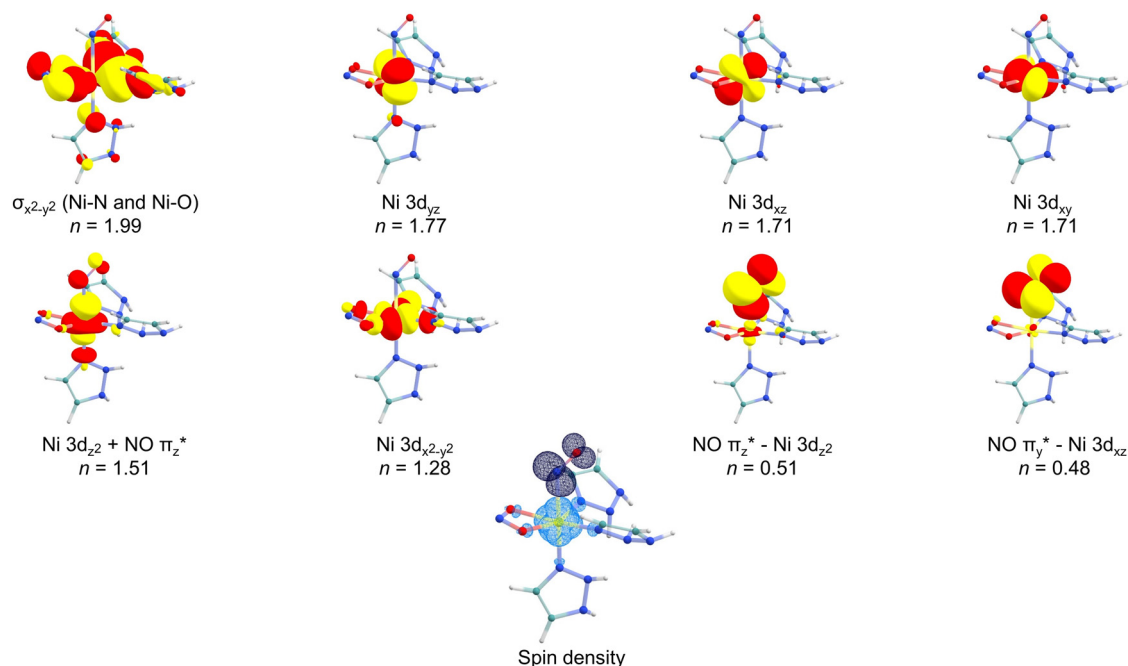
Fig. 8 Contour plots of the most important natural orbitals (with predominant Ni 3d and NO π* character) optimized with the CASSCF(11e,11o) calculation and spin density map. Indicated qualitative nature and fractional occupation number (n) are reported. Contour values: ±0.03 a.u. for the orbitals and ± 0.003 electrons/a_0 for the spin density (the positive sign is shown in cyan, the negative sign in dark blue). N, O, Ni, C and H atoms are reported in blue, red, yellow, green and white, respectively.

The rhombic g-tensor is correctly reproduced, and the trend $g_{zz} > g_{yy} > g_{xx}$, is detected experimentally for the main Ni^{II}–NO species validating the microscopic structure proposed in Fig. 7. The computed orientation of the z principal axis of the g-tensor is approximately perpendicular with respect to the plane defined by the $d_{x^2-y^2}$ orbital, as it typically happens when the unpaired electron is in the $d_{x^2-y^2}$ orbital. Overall, the computed quadrupole interaction for the different nitrogen nuclei is in reasonable agreement with the experimental findings.

The computed spin Hamiltonian parameters for the nitrogen ligands directly bound to Ni may be grouped into two families of nitrogen nuclei, in agreement with ENDOR experiments. N_{f1}, N_{f2} and N_{f3} possess almost identical hyperfine and quadrupole couplings which nicely fit with the experimental values found for $^{14}N(2)$. Moreover, they are characterized by Euler angles different from each other (Table S2, ESI†). A spectral simulation of the ENDOR spectra obtained by using the calculated Euler angles for N_{f1}, N_{f2} and N_{f3} is reported in Fig. S9 (ESI†) confirming that, by considering nitrogen nuclei with similar spin Hamiltonian parameters but different orientation of the hyperfine and quadrupole tensors (as predicted by quantum chemical calculations), a satisfying explanation of the

features of the low-frequency spectra may be obtained. This permits to assign $^{14}N(2)$ species to nitrogen atoms from the SBU, forming a σ-bond with the nickel center. On the other hand, $^{14}N(1)$ signal is consistent with the computed ^{14}N hyperfine couplings from the NO ligand, which correctly reproduces the large dipolar contribution. The weak ^{14}N hf interaction detected by HYSCORE experiments is instead consistent with the ones calculated for nitrogen atoms of the benzobistriazolate immediately close to the nitrogen linked to the nickel (N_s in Fig. 7).

Although the binding mechanism of NO to Ni^{II} ion occurs through the same way (*e.g.* spin pairing mechanism) regardless the nature of the embedding considered, there are substantial structural and magnetic differences between the Ni^{II}–NO adduct described here and the ones reported for other microporous systems. Table 3 summarizes the main structural, electronic and magnetic differences between the nickel–nitrosyl complex in this work and the one recently characterized by Pietrzyk *et al.*[14] in zeolite-type material. Apart from the different coordination geometry (pseudo-octahedral instead of square pyramidal), the Ni–NO bond distance is longer while the N–O bond length is slightly shorter compared to what is reported for

Table 3 Calculated bond length (d in nm), computed spin populations (%) at Ni (ρ_{Ni}) and NO ligand (ρ_{NO}) and experimental maximum ^{14}N hyperfine couplings ($A_{max} = |a_{iso} + 2T|$, in MHz) of Ni^{II}–NO moieties detected in this work and in Ni-doped ZSM-5 system. The data relative to ZSM-5 are taken from Pietrzyk *et al.*[14]

	System	Geometry	$d_{Ni–NO}$	$d_{N–O}$	ρ_{Ni}	ρ_{NO}	$^N A_{max}$	Ref.
Ni^{II}–NO in MFU-4l	MOF	Pseudo-octahedral	0.230	0.114	+1.55	−0.35	29.0	This work
Ni^{II}–NO in ZSM-5	Zeolite	Square pyramidal	0.190	0.117	+1.22	−0.27	14.0	14

This journal is © the Owner Societies 2023

Phys. Chem. Chem. Phys., 2023, **25**, 15702–15714 | **15711**

Ni-ZSM-5 material.[14] This is consistent with a weaker NO associative mechanism agreeing with the lower NO adsorption energy reported here compared to zeolite case. Such tiny structural details affect the electronic structure and, thus, the EPR parameters. Because of the shorter N–O bond, the NO ligand acquires a partial positive charge. The cationic resonance structure ($Ni^I(S = 1/2) - NO^+$) has a higher contribution (8.9%) compared to the case in ZSM-5 (6.3%) in the description of the ground state. Consequently, the positive spin population on the Ni ion as well as the negative spin population on the NO ligand – induced by spin polarization – are larger than the ones reported by Pietrzyk (see Table 3). The experimental ^{14}N hyperfine couplings of the nitrosyl ligand clearly reflect the changes in spin distribution whereby larger hf interactions are detected in MFU-4l-NO$_2$ compared to ZSM-5 case.

Conclusion

EPR spectroscopy and quantum chemical calculations were carried out to assess the geometric and electronic structure of Ni^{II}–NO moieties in Ni^{II}-MFU-4l-NO$_2$ material. W-band CW-EPR detected five-coordinated Ni^{II} species assigned to the peripheral sites of the parent Ni-MFU-4l-NO$_2$, MOF in agreement with DFT calculations. Such divalent nickel centers are capable of chemoselective capture of gaseous NO-forming mononitrosyl complexes with electron spin $S = 1/2$, which can be easily identified by CW X-band EPR measurements. The nature of the Ni^{II}–NO bond and of the Ni–N$_f$ bonds was ascertained by ENDOR studies and thoroughly accounted for by DFT/CASSCF calculations. While the bonding of Ni with N$_f$ ligands from the SBU is characterized by a direct spin density transfer via overlap of the nitrogen sp orbitals with the nickel $3d_{x^2-y^2}$ orbital, the NO bonding is due to spin pairing mechanism NO↑ + Ni^{II}↑↑ → [↑Ni^{II}(↑ ↓)NO] whereby the transfer of spin density arises via spin polarization of the NO π orbital perpendicular to the Ni $3d_{x^2-y^2}$ orbital. The results presented here highlight the capabilities of sophisticated EPR techniques in combination with quantum chemical calculations in providing fundamental insights into the non-obvious electronic structure of open-shell species docked in metal–organic frameworks.

Abbreviations

EPR	Electron paramagnetic resonance
HYSCORE	Hyperfine sublevel correlation spectroscopy
DFT	Density functional theory
MOF	Metal–organic framework
ESEEM	Electron spin echo envelope modulation
ENDOR	Electron nuclear double resonance

Author contributions

The manuscript was written through the contributions of all authors. All authors have given approval for the final version of the manuscript.

Conflicts of interest

There are no conflicts to declare.

References

1 M. Chiesa, E. Giamello and M. Che, *Chem. Rev.*, 2010, **110**(3), 1320.
2 L. Andrews and A. Citra, *Chem. Rev.*, 2002, **102**(4), 885.
3 K. Hadjiivanov, *Catal. Rev.: Sci. Eng.*, 2000, **42**(1–2), 71.
4 Z. Sojka, M. Che and E. Giamello, *J. Phys. Chem. B*, 1997, **101**(24), 4831.
5 G. Spoto, A. Zecchina, S. Bordiga, G. Ricchiardi, G. Martra, G. Leofanti and G. Petrini, *Appl. Catal.*, 1994, **3**(2–3), 151.
6 E. Giamello, D. Murphy, G. Magnacca, C. Morterra, Y. Shioya, T. Nomura and M. Anpo, *J. Catal.*, 1992, **136**(2), 510.
7 F. Witzel, H. G. Karge, A. Gutsze and U. Hartel, *Chem.-Ing.-Tech.*, 1991, **63**, 744.
8 T. Rudolf, W. Böhlmann and A. Pöppl, *J. Magn. Reson.*, 2002, **155**(1), 45.
9 M.-T. Nechita, G. Berlier, G. Ricchiardi, S. Bordiga and A. Zecchina, *Catal. Lett.*, 2005, **103**(1–2), 33.
10 A. Pöppl, T. Rudolf, P. Manikandan and D. Goldfarb, *J. Am. Chem. Soc.*, 2000, **122**(41), 10194.
11 A. Pöppl, T. Rudolf and D. Michel, *J. Am. Chem. Soc.*, 1998, **120**(19), 4879.
12 V. Umamaheswari, M. Hartmann and A. Pöppl, *Magn. Reson. Chem.*, 2005, **43**, S205–14.
13 P. Fisicaro, E. Giamello, G. Berlier and C. Lamberti, *Res. Chem. Intermed.*, 2003, **29**(7–9), 805.
14 P. Pietrzyk, K. Góra-Marek, T. Mazur, B. Mozgawa, M. Radoń, M. Chiesa, Z. Zhao and Z. Sojka, *J. Catal.*, 2021, **394**, 206.
15 S. Jensen, K. Tan, L. Feng, J. Li, H.-C. Zhou and T. Thonhauser, *J. Am. Chem. Soc.*, 2020, **142**(39), 16562.
16 M. Ahrens, O. Marie, P. Bazin and M. Daturi, *J. Catal.*, 2010, **271**(1), 1.
17 W. Schießer, H. Vinek and A. Jentys, *Appl. Catal.*, 2001, **33**(3), 263.
18 P. C. Ford and I. M. Lorkovic, *Chem. Rev.*, 2002, **102**(4), 993.
19 J. A. McCleverty, *Chem. Rev.*, 2004, **104**(2), 403.
20 G. R. A. Wyllie and W. R. Scheidt, *Chem. Rev.*, 2002, **102**(4), 1067.
21 V. Umamaheswari, M. Hartmann and A. Pöppl, *J. Phys. Chem. B*, 2005, **109**(42), 19723.

15712 | *Phys. Chem. Chem. Phys.*, 2023, **25**, 15702–15714

This journal is © the Owner Societies 2023

22 H. Yahiro, A. Lund and M. Shiotani, *Spectrochim. Acta, Part A*, 2004, **60**(6), 1267.

23 M. Chiesa and E. Giamello, *Catal. Lett.*, 2021, **151**(12), 3417.

24 P. Pietrzyk and Z. Sojka, EPR spectroscopy and DFT calculations of the g tensors of {VO}1/ZSM-5, {CuNO}11/ZSM-5 and {NaNO}1/ZSM-5 intrazeolitic complexes, in *Studies in Surface Science and Catalysis: Molecular Sieves: From Basic Research to Industrial Applications*, ed. J. Čejka, N. Žilková, P. Nachtigall, Elsevier, 2005. pp. 617–624.

25 Z. Sojka and P. Pietrzyk, *Spectrochim. Acta, Part A*, 2004, **60**(6), 1257.

26 P. Pietrzyk and Z. Sojka, *J. Phys. Chem. A*, 2005, **109**(46), 10571.

27 K. Podolska-Serafin and P. Pietrzyk, *J. Mol. Struct.*, 2019, **1180**, 754.

28 M. Gutjahr, R. Böttcher and A. Pöppl, *J. Phys. Chem. B*, 2002, **106**(6), 1345.

29 B. Barth, M. Mendt, A. Pöppl and M. Hartmann, *Microporous Mesoporous Mater.*, 2015, **216**, 97.

30 M. Mendt, B. Barth, M. Hartmann and A. Pöppl, *J. Chem. Phys.*, 2017, **147**(22), 224701.

31 M. Mendt, F. Gutt, N. Kavoosi, V. Bon, I. Senkovska, S. Kaskel and A. Pöppl, *J. Phys. Chem. C*, 2016, **120**(26), 14246.

32 B. Jee, K. Koch, L. Moschkowitz, D. Himsl, M. Hartman and A. Pöppl, *J. Phys. Chem. Lett.*, 2011, **2**(5), 357.

33 E. Giamello, E. Garrone, E. Guglielminotti and A. Zecchina, *J. Mol. Catal.*, 1984, **24**(1), 59.

34 M. Chiesa, *J. Mol. Catal. A: Chem.*, 2003, **204–205**, 779.

35 D. Denysenko, M. Grzywa, M. Tonigold, B. Streppel, I. Krkljus, M. Hirscher, E. Mugnaioli, U. Kolb, J. Hanss and D. Volkmer, *Chem. – Eur. J.*, 2011, **17**(6), 1837.

36 S. Biswas, M. Grzywa, H. P. Nayek, S. Dehnen, I. Senkovska, S. Kaskel and D. Volkmer, *Dalton Trans.*, 2009, 6487.

37 D. Denysenko, J. Jelic, K. Reuter and D. Volkmer, *Chem. – Eur. J.*, 2015, **21**(22), 8188.

38 D. Denysenko and D. Volkmer, *Faraday Tras.*, 2017, **201**, 101.

39 S. Stoll and A. Schweiger, *J. Magn. Reson.*, 2006, **178**(1), 42.

40 P. Höfer, A. Grupp, H. Nebenführ and M. Mehring, *Chem. Phys. Lett.*, 1986, **132**(3), 279.

41 E. R. Davies, *Phys. Lett. A*, 1974, **47**(1), 1.

42 D. Denysenko, M. Grzywa, J. Jelic, K. Reuter and D. Volkmer, *Angew. Chem.*, 2014, **53**(23), 5832.

43 R. Dovesi, A. Erba, R. Orlando, C. M. Zicovich-Wilson, B. Civalleri, L. Maschio, M. Rérat, S. Casassa, J. Baima, S. Salustro and B. Kirtman, *Comput. Mol. Sci.*, 2018, **8**(4), e1360.

44 A. Erba, J. Baima, I. Bush, R. Orlando and R. Dovesi, *J. Chem. Theory Comput.*, 2017, **13**(10), 5019.

45 C. Lee, W. Yang and R. B. Parr, *Phys. Rev. B: Condens. Matter Mater. Phys.*, 1988, **37**(2), 785.

46 A. D. Becke, *J. Chem. Phys.*, 1993, **98**(7), 5648.

47 S. Grimme, J. Antony, S. Ehrlich and H. Krieg, *J. Chem. Phys.*, 2010, **132**(15), 154104.

48 S. Grimme, S. Ehrlich and L. Goerigk, *J. Comput. Chem.*, 2011, **32**(7), 1456.

49 D. Vilela Oliveira, J. Laun, M. F. Peintinger and T. Bredow, *J. Comput. Chem.*, 2019, **40**(27), 2364.

50 K. Eichkorn, F. Weigend, O. Treutler and R. Ahlrichs, *Theor. Chem. Acta.*, 1997, **97**(1–4), 119.

51 C. M. Zicovich-Wilson, F. Pascale, C. Roetti, V. R. Saunders, R. Orlando and R. Dovesi, *J. Comput. Chem.*, 2004, **25**(15), 1873.

52 F. Pascale, C. M. Zicovich-Wilson, F. López Gejo, B. Civalleri, R. Orlando and R. Dovesi, *J. Comput. Chem.*, 2004, **25**(6), 888.

53 C. Carteret, M. de La Pierre, M. Dossot, F. Pascale, A. Erba and R. Dovesi, *J. Chem. Phys.*, 2013, **138**(1), 14201.

54 F. Neese, *Wiley Interdiscip. Rev.: Comput. Mol. Sci.*, 2022, **12**(5).

55 C. Remenyi, R. Reviakine, A. V. Arbuznikov, J. Vaara and M. Kaupp, *J. Phys. Chem. A*, 2004, **108**(23), 5026.

56 B. A. Heß, C. M. Marian, U. Wahlgren and O. Gropen, *Chem. Phys. Lett.*, 1996, **251**(5–6), 365.

57 S. Grimme, *J. Chem. Phys.*, 2006, **124**(3), 34108.

58 F. Weigend and R. Ahlrichs, *Phys. Chem. Chem. Phys.*, 2005, **7**(18), 3297.

59 J. L. Whitten, *J. Chem. Phys.*, 1973, **58**(10), 4496.

60 F. Weigend, *Phys. Chem. Chem. Phys.*, 2006, **8**(9), 1057.

61 G. L. Stoychev, A. A. Auer and F. Neese, *J. Chem. Theory Comput.*, 2017, **13**(2), 554.

62 V. Barone, *J. Phys. Chem.*, 1995, **99**(30), 11659.

63 J. P. S. Walsh, S. Sproules, N. F. Chilton, A.-L. Barra, G. A. Timco, D. Collison, E. J. L. McInnes and R. E. P. Winpenny, *Inorg. Chem.*, 2014, **53**(16), 8464.

64 K. Amrutha and V. Kathirvelu, *J. Phys. Chem. Solids*, 2021, **157**, 110224.

65 C. R. Wilson, M. J. Riley, D. Wang and G. R. Hanson, *Chem. Phys.*, 1997, **217**(1), 63.

66 K. Amrutha and V. Kathirvelu, *Magn. Reson. Chem.*, 2022, **60**(3), 414.

67 J. Krzystek, J.-H. Park, M. W. Meisel, M. A. Hitchman, H. Stratemeier, L.-C. Brunel and J. Telser, *Inorg. Chem.*, 2002, **41**(17), 4478.

68 J. Krzystek, A. Ozarowski and J. Telser, *Coord. Chem. Rev.*, 2006, **250**(17–18), 2308.

69 J. Krzystek, S. A. Zvyagin, A. Ozarowski, S. Trofimenko and J. Telser, *J. Magn. Reson.*, 2006, **178**(2), 174.

70 J. Lu, I. O. Ozel, C. A. Belvin, X. Li, G. Skorupskii, L. Sun, B. K. Ofori-Okai, M. Dincă, N. Gedik and K. A. Nelson, *Chem. Sci.*, 2017, **8**(11), 7312.

71 D. Collison, M. Helliwell, V. M. Jones, F. E. Mabbs, E. J. L. McInnes, P. C. Riedi, G. M. Smith, R. G. Pritchard and W. I. Cross, *Faraday Tras.*, 1998, **94**(19), 3019.

72 P. J. van Dam, A. A. K. Klaassen, E. J. Reijerse and W. R. Hagen, *J. Magn. Reson.*, 1998, **130**(1), 140.

73 J. Mroziński, A. Skorupa, A. Pochaba, Y. Dromzée, M. Verdaguer, E. Goovaerts, H. Varcammen and B. Korybut-Daszkiewicz, *J. Mol. Struct.*, 2001, **559**(1–3), 107.

74 L. A. Pardi, A. K. Hassan, F. B. Hulsbergen, J. Reedijk, A. L. Spek and L. C. Brunel, *Inorg. Chem.*, 2000, **39**(2), 159.

75 S.-D. Jiang, D. Maganas, N. Levesanos, E. Ferentinos, S. Haas, K. Thirunavukkuarasu, J. Krzystek, M. Dressel, L. Bogani, F. Neese and P. Kyritsis, *J. Am. Chem. Soc.*, 2015, **137**(40), 12923.

76 A. Kubica, J. Kowalewski, D. Kruk and M. Odelius, *J. Chem. Phys.*, 2013, **138**(6), 64304.

This journal is © the Owner Societies 2023

Phys. Chem. Chem. Phys., 2023, **25**, 15702–15714 | **15713**

77 F. Neese, *Coord. Chem. Rev.*, 2009, **253**(5–6), 526.

78 S. Ye and F. Neese, *Inorg. Chem.*, 2010, **49**(3), 772.

79 F. Neese, *J. Am. Chem. Soc.*, 2006, **128**(31), 10213.

80 W. Hayes and J. Wilkens, *Proc. R. Soc. Lond. A*, 1964, **281**(1386), 340.

81 A. Abragam and B. Bleaney, *Electron paramagnetic resonance of transition ions*, Dover Publications, New York, 1986.

82 N. M. Atherton, *Ellis Horwood and PTR Prentice Hall*, *eMagRes*, 1993.

83 J. R. Harmer, Hyperfine Spectroscopy – ENDOR, *eMagRes*, John Wiley & Sons, Ltd, 2016. pp. 1493–514.

84 J. A. J. Fitzpatrick, F. R. Manby and C. M. Western, *J. Chem. Phys.*, 2005, **122**, 084312.

85 W. B. Mims and J. Peisach, *J. Chem. Phys.*, 1978, **69**(11), 4921.

86 V. K. K. Praneeth, F. Neese and N. Lehnert, *Inorg. Chem.*, 2005, **44**(8), 2570.

87 C. Wäckerlin, D. Chylarecka, A. Kleibert, K. Müller, C. Iacovita, F. Nolting, T. A. Jung and N. Ballav, *Nat. Commun.*, 2010, **1**(1), 61.

88 C. Daniel and C. Gourlaouen, *Mol.*, 2019, **24**(20), 3638.

89 J. H. Enemark and R. D. Feltham, *J. Am. Chem. Soc.*, 1974, **96**(15), 5002.

90 R. D. Feltham and J. H. Enemark, Structures of Metal Nitrosyls, in *Geoffroy, editor. Topics in inorganic and organo-metallic stereochemistry. Topics in Stereochemistry*, John Wiley, 1981, vol. 12, pp. 155–215.

91 J. H. Enemark and R. D. Feltham, *Coord. Chem. Rev.*, 1974, **13**(4), 339.

92 R. Hoffmann, M. M. L. Chen, M. Elian, A. R. Rossi and D. M. P. Mingos, *Inorg. Chem.*, 1974, **13**(11), 2666.

93 W. R. Scheidt, K. Hatano, G. A. Rupprecht and P. L. Piciulo, *Inorg. Chem.*, 1979, **18**(2), 292.

94 E. A. Dierks, S. Hu, K. M. Vogel, A. E. Yu, T. G. Spiro and J. N. Burstyn, *J. Am. Chem. Soc.*, 1997, **119**(31), 7316.

95 A. Stępniewski, M. Radoń, K. Góra-Marek and E. Broclawik, *Phys. Chem. Chem. Phys.*, 2016, **18**(5), 3716.

96 M. Radoń, E. Broclawik and K. Pierloot, *J. Phys. Chem. B*, 2010, **114**(3), 1518.

97 L. Freitag, S. Knecht, C. Angeli and M. Reiher, *J. Chem. Theory Comput.*, 2017, **13**(2), 451.

98 T. Ampßler, G. Monsch, J. Popp, T. Riggenmann, P. Salvador, D. Schröder and P. Klüfers, *Angew. Chem.*, 2020, **59**(30), 12381.

99 J. K. Bower, A. Y. Sokolov and S. Zhang, *Angew. Chem.*, 2019, **58**(30), 10225.

15714 | *Phys. Chem. Chem. Phys.*, 2023, **25**, 15702–15714

This journal is © the Owner Societies 2023